nature materials

ARTICLES

PUBLISHED ONLINE: 24 NOVEMBER 2013 | DOI: 10.1038/NMAT3793

Detection of subsurface structures underneath dendrites formed on cycled lithium metal electrodes

Katherine J. Harry[1,2], Daniel T. Hallinan[3], Dilworth Y. Parkinson[4], Alastair A. MacDowell[4] and Nitash P. Balsara[2,3,5]*

Failure caused by dendrite growth in high-energy-density, rechargeable batteries with lithium metal anodes has prevented their widespread use in applications ranging from consumer electronics to electric vehicles. Efforts to solve the lithium dendrite problem have focused on preventing the growth of protrusions from the anode surface. Synchrotron hard X-ray microtomography experiments on symmetric lithium–polymer–lithium cells cycled at 90 °C show that during the early stage of dendrite development, the bulk of the dendritic structure lies within the electrode, underneath the polymer/electrode interface. Furthermore, we observed crystalline impurities, present in the uncycled lithium anodes, at the base of the subsurface dendritic structures. The portion of the dendrite protruding into the electrolyte increases on cycling until it spans the electrolyte thickness, causing a short circuit. Contrary to conventional wisdom, it seems that preventing dendrite formation in polymer electrolytes depends on inhibiting the formation of subsurface structures in the lithium electrode.

Reliable, rechargeable batteries with a high specific energy are vital for a wide variety of applications[1]. From many perspectives, the most attractive anode for a rechargeable battery is lithium metal because it is the lightest and most electropositive metal[2,3]. A major problem that emerges when batteries containing a lithium metal anode are cycled is the growth of dendrites that seem to protrude from the lithium metal surface[4,5]. The passage of current through these structures can result in ignition of the electrolyte and catastrophic failure[6,7]. Efforts to prevent dendrite growth have primarily focused on blocking these protrusions[8–11]. This Article demonstrates the presence of subsurface structures within the lithium electrode that lie underneath the dendrites. Furthermore, the formation of the subsurface structures dominates early stages of dendrite growth in polymer electrolyte cells at 90 °C, suggesting that the key to preventing dendrite formation is the elimination of filamentous cavities inside the electrode.

The electrodes in today's lithium ion batteries are porous, and about 30 vol% of the electrode is taken up by inactive phases[12]. With a lithium metal anode however, the simplicity of the reactions at the lithium electrode and facile transport of electrons within the metal eliminates the need for designing porous electrodes containing separate phases for transporting ions and electrons. Furthermore, many of the high-energy-density battery technologies being researched today, such as lithium–sulphur and lithium–air batteries, assume the presence of a lithium metal anode[13,14]. It is thus not surprising that researchers have used a variety of tools to study dendrite formation in lithium batteries. These include optical and electron microscopy[15–20], nuclear magnetic resonance[21], magnetic resonance imaging[22] and so on. These techniques have detected 'tree-like' or 'moss-like' structures that emanate from the lithium surface and protrude into the electrolyte[23–25]. A key advance in this Article is the use of synchrotron hard X-ray microtomography that enables the imaging of structures residing on either side of the lithium metal electrode/electrolyte interface, illuminating the presence of subsurface structures in the lithium anode beneath dendritic protrusions.

The cells used in these experiments are symmetric lithium–polymer–lithium cells assembled and pouched inside an argon-filled glovebox. The polymer electrolyte was a polystyrene-block-poly(ethylene oxide) copolymer (SEO) mixed with lithium bis(trifluoromethanesulfonyl)imide (LiTFSI) salt. Details about the procedure used to prepare the electrolyte film are given in the Methods. Two 150-μm-thick, 8-mm-diameter lithium electrodes were punched out of lithium foil (FMC lithium). One 10-mm-diameter piece of copolymer electrolyte was punched out of the prepared 30-μm-thick film and sandwiched between the lithium electrodes. Nickel current collector tabs were placed on the electrodes and the whole cell was vacuum sealed in a polypropylene lined, aluminium pouch. The cells were cycled in an oven at 90 °C using a Bio-Logic VMP3 potentiostat at atmospheric pressure.

The cycling routine for all cells was as follows. Each cycle consisted of a 4 h charge followed by a 45 min rest and a 4 h discharge. The cells were first cycled 15 times at a low current density of 0.02 mA cm^{-2}. This was followed by cycling at a current density of 0.175 mA cm^{-2} until the experiment was stopped for cell imaging or when the cell shorted. A typical cycling routine is shown in Supplementary Fig. 1 where the time dependence of the measured cell voltage and the applied current is shown.

After cycling, the cells were taken back into the glovebox where a 3 mm punch was used to remove a small portion of the cell for imaging. In addition, the nickel current collectors were removed. The smaller cell size and elimination of the nickel current collectors improved the quality of the X-ray microtomography images. The punched out portion of the cell was vacuum sealed in a pouch and transferred from the glovebox to the microtomography beamline.

[1]Department of Materials Science and Engineering, University of California, Berkeley, California 94720, USA, [2]Materials Science Division, Lawrence Berkeley National Laboratory, Berkeley, California 94720, USA, [3]Environmental Energy Technology Division, Lawrence Berkeley National Laboratory, Berkeley, California 94720, USA, [4]Advanced Light Source Division, Lawrence Berkeley National Laboratory, Berkeley, California 94720, USA, [5]Department of Chemical and Biomolecular Engineering, University of California, Berkeley, California 94720, USA. *e-mail: nbalsara@berkeley.edu

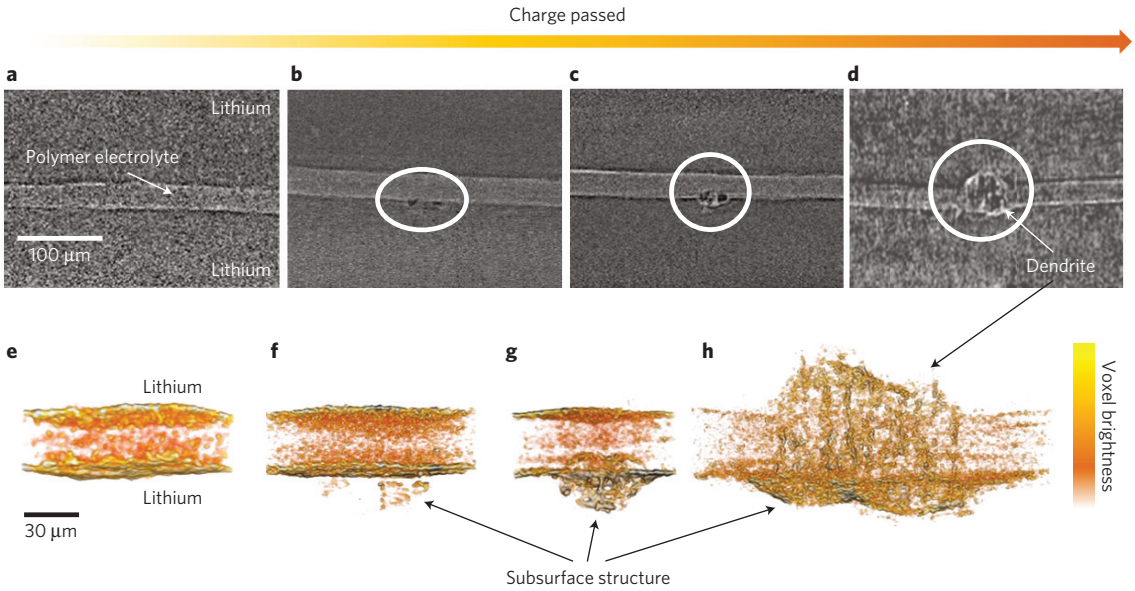

Figure 1 | Evolution of dendrite growth. a–d, X-ray tomography slices showing the cross-sections of symmetric lithium cells cycled to various stages. The thin, bright horizontal strip through the centre of the images is the polystyrene-block-poly(ethylene oxide) copolymer electrolyte sandwiched between two lithium metal electrodes. The amount of charge passed, C, for each cell is: 0 C cm^{-2} (**a**), 9 C cm^{-2} (**b**) and 84 C cm^{-2} (**c**). **d**, Shorted cell: 296 C cm^{-2}. Dendritic structures are evident in **b–d**. **e–h**, Magnified, 3D reconstructed volumes of cells shown in the top panel. **e**, An uncycled cell with no dendritic structures, $C = 0$ C cm^{-2}. **f**, Heterogeneous structures begin to form in the bottom electrode in early stages of cycling, $C = 9$ C cm^{-2}. **g**, Dendritic structures in both electrolyte and electrode phases are seen at the intermediate stage of cycling, $C = 84$ C cm^{-2}. **h**, Dendritic structures that span the thickness of the electrolyte are seen in the shorted cell, $C = 296$ C cm^{2}. The arrow indicates the colour scale for voxel brightness.

The cells were imaged using hard X-ray microtomography at the Advanced Light Source at Lawrence Berkeley National Laboratory[26]. Slices through typical tomograms obtained from our cells are shown in Fig. 1. Figure 1a shows an image obtained from an uncycled cell. The image is dominated by three phases, two lithium electrodes that surround a 30-µm-thick electrolyte. As both the electrolyte and the electrodes are composed of light elements, the tomography data mainly reflect the interface between these phases. The electrode/electrolyte interfaces of uncycled cells are devoid of any noticeable features (Fig. 1a). We examined four uncycled cells with a total electrode/electrolyte interface of 12 mm^2 and found no dendritic structures. Figure 1b shows an image of a cell after 15 conditioning cycles at 0.02 mA cm^{-2} ($C = 9$ C cm^{-2}). The image shows the presence of heterogeneities in the lower lithium electrode. The entire cell at this stage had six identifiable heterogeneous structures located in both electrodes. Figure 1c shows an image of an unshorted cell after the conditioning cycles and an additional 15 cycles at the full current density of 0.175 mA cm^{-2} (the total amount of charge passed, $C = 84$ C cm^{-2}). Numerous dendritic structures were seen in the cell. The bottom electrode in Fig. 1c shows one example. No electrolyte-spanning structures were seen in this cell. Figure 1d shows an image of a shorted cell after 63 full cycles at 0.175 mA cm^{-2} ($C = 296$ C cm^{-2}). Shorted cells showed dendritic structures that were bigger than those shown in Fig. 1c. They also showed electrolyte-spanning structures and an example is shown in Fig. 1d. Videos showing the full tomogram of the cells shown in Fig. 1 are available in the Supplementary Information. In a given cell, dendrite growth was observed on both electrodes with roughly equivalent prevalence. For simplicity, the images in Fig. 1 are oriented so that the dendritic structures are in the bottom electrode.

The bottom panel of Fig. 1 shows three-dimensional (3D) reconstructed volumes of selected regions around the slices shown in the top panel. Each reconstructed volume may be viewed as a 3D array of brightness values. Voxels with a brightness below a certain threshold were rendered transparent and the rest were placed on a colour scale with yellow indicating the brightest voxels. The voxel brightness is proportional to the local electron density, and the electrolyte/electrode interface is highlighted by Fresnel phase contrast[27,28]. In addition, the data were subjected to an edge-enhancement protocol wherein the change in voxel intensity with position is recorded and areas where these changes are steep are highlighted in black. All of the analysis described above was conducted using the commercial image processing package Avizo.

The 3D nature of the dendritic structures formed in our cells is clearly evident in the bottom panel of Fig. 1. In Fig. 1e, we mainly see two flat sheets representing the uncycled electrode/electrolyte interfaces. X-ray absorption is higher for the SEO electrolyte than the lithium electrode, resulting in brighter voxels in the electrolyte phase. The presence of dark orange features between the sheets in Fig. 1e and the absence of features above and below the sheets is due to this effect. The resolution of this imaging technique is of the order of a micrometre. Some speckling is visible in the images due to noise. The lightly cycled cell shown in Fig. 1f ($C = 9$ C cm^{-2}) exhibits orange features below the bottom electrode/electrolyte interface. Figure 1g shows the reconstructed volume of the dendritic structure seen in Fig. 1c ($C = 84$ C cm^{-2}). The dendritic structure has two parts, one that lies within the electrolyte and the other that lies within the electrode. As our imaging technique highlights interfaces, it is evident that both parts of the dendrites are filled with ramified lithium/polymer interfaces.

As one expects dendrites to be filamentous structures, the presence of lithium/polymer interfaces on the electrolyte side is not surprising. The presence of filamentous structures on the electrode side is the surprising new finding of this study. It is clear that most of the dendrite in Fig. 1g resides within the electrode, not within the electrolyte. Figure 1h shows a reconstructed volume of the electrolyte-spanning dendritic structure pictured in Fig. 1d. Here we see lithium–polymer interfaces that run across the electrolyte and the presence of filamentous structures in both top and bottom electrodes.

For the case of the non-electrolyte-spanning dendritic structures, (for example, Fig. 1c), we approximate the volume of the

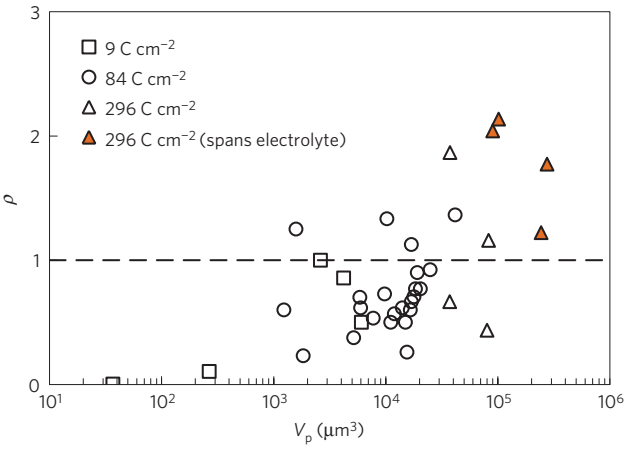

Figure 2 | Shift of dendrite volume fraction from electrode to electrolyte. Properties of dendritic structures obtained from three cells with $C = 9$, 84 and 296 C cm^{-2}. The ratio of the volume of the dendritic structure in the polymer electrolyte to the volume of the structure in the electrode (ρ) is plotted against the volume of the dendritic structure in the polymer electrolyte (V_p). In the initial stages of cycling ($C = 9$ C cm^{-2}), most of the data points lie below the $\rho = 1$ line indicating that most of the dendritic structures in these cases lie within the electrode. As the dendrites develop and V_p increases, the portion of the structure extending into the electrolyte grows until the dendritic structure spans the electrolyte, resulting in cell failure.

structure that lies in the electrolyte and the part that lies in the electrode as two half-ellipsoids. The method used to quantify the volume of the dendritic structures that lie in the electrode or in the electrolyte is explained in detail in the Methods. We define ρ to be the ratio of the volume of the dendritic structure in the electrolyte to the volume in the electrode. Figure 2 shows a plot of ρ versus V_p, the volume of the dendritic structure in the polymer electrolyte, for three cells cycled to different values of C. Data obtained at different stages of cycling are identified by different symbols. The values of ρ of all of the dendritic structures obtained during the early stage of cycling ($C = 9$ C cm^{-2}) are equal to or less than unity. The average value of ρ for this data set is 0.4, indicating that the dendritic structures lie mostly within the electrode. The values of ρ obtained at the intermediate stage of cycling ($C = 84$ C cm^{-2}) scatter between 0.2 and 1.4 but 19 out of the 23 dendritic structures observed have values of ρ less than unity. The average value of ρ for this data set is 0.7, indicating that even at this stage, the dendritic structures lie mostly within the electrode. Half of the dendritic structures obtained in the shorted cell spanned the electrolyte (Fig. 1d). We approximate these structures as elliptic cylinders that run through the electrolyte capped by two half-ellipsoids. The methodology to determine ρ for these structures is analogous to that described in the Supplementary Information. Most of the values of ρ obtained in the shorted cell are greater than one (average value of ρ is 1.4), indicating that in this stage the dendritic structures lie mostly in the electrolyte.

Figure 3a,b shows a reconstructed 3D volume of a portion of a cell that contained two dendritic structures near each other obtained during the intermediate stage of cycling. (This is a different portion of the same cell shown in Fig. 1c,g.) After X-ray imaging, the cell shown in Fig. 3a,b was brought back into an argon-filled glovebox where it was submerged in a 1:9 by volume mixture of tetrahydrofuran and benzene for two weeks. The polymer electrolyte dissolved away, enabling the imaging of the lithium electrodes using scanning electron microscopy (SEM). The presence of two dendritic structures near each other was rare and thus it was relatively easy to identify the portion of the electrode from which

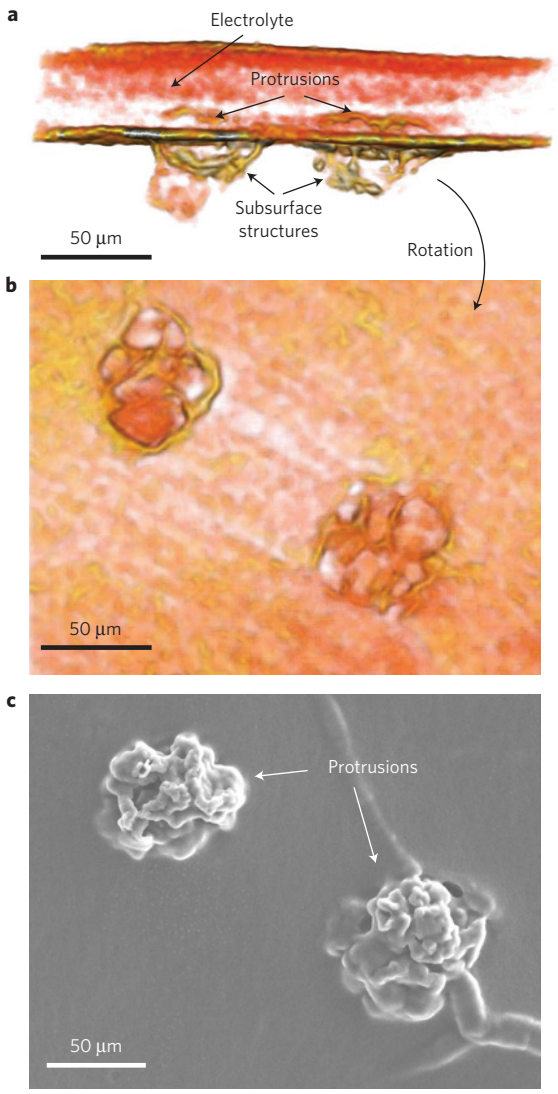

Figure 3 | Comparison of 3D reconstructions with SEM. a, 3D reconstructed volume of a cell with $C = 84$ C cm^{-2} containing two, closely spaced dendrites. **b**, The reconstructed volume was rotated such that the viewer is within the electrolyte looking at the dendrites. **c**, SEM micrograph of the bottom electrode of the same cell, after dissolving away the electrolyte, showing the dendritic structures. The SEM images contain no direct evidence for the presence of subsurface structures under the dendritic protrusions.

the reconstructed 3D volume was obtained in the scanning electron microscope. The SEM image thus obtained is shown in Fig. 3c. The dendrites seen in this image are similar to structures reported in the literature[2,20]. In particular there is only a hint of the existence of a subsurface structure underneath these dendritic structures. Figure 3a provides a more complete description of these dendritic structures. The values of ρ for these dendritic structures are 0.7 and 0.6, indicating that large portions of the dendritic structures imaged in Fig. 3c lie beneath the electrode/electrolyte interface and are not visible in the SEM image.

It is important to determine whether the characteristics of dendritic structures reported above apply only to nanostructured electrolytes. This was addressed by conducting experiments on a symmetric lithium–lithium cell with a mixture of polyethylene oxide (PEO) homopolymer and LiTFSI as the electrolyte. The average electrolyte thickness in this cell was 200 μm, which is considerably larger than that of the SEO electrolytes described

above. We were unable to create thin PEO-based electrolytes in our laboratory. The ability to create thin films is a strong function of the mechanical properties of the material, and the modulus of SEO electrolytes is a factor of about 100 larger than that of PEO (ref. 18). We used a slightly different cycling protocol for this cell from that used for SEO cells owing to the electrolyte thickness difference as described in the Methods. The dendritic structure observed by X-ray microtomography after the cell shorted is shown in Supplementary Fig. 2. Subsurface structures were clearly observed in this case. Although the detailed shape and location of the dendritic structures depend on a variety of experimental parameters such as thickness, modulus and morphology of the electrolyte, current density, and total amount of charge passed per cycle, subsurface structures were observed in all of the experiments conducted thus far. Supplementary Fig. 3 shows the effect of the total amount of charge passed per cycle on dendrite morphology.

The mechanism by which the dendritic structures shown in Fig. 1 nucleate and grow is an important question that we cannot definitively answer at this stage. In the future we will address this issue by conducting *in situ* X-ray microtomography experiments during cycling. Our hypothesis at this juncture is that contaminants in the lithium electrode are responsible for the nucleation of subsurface dendritic structures. The manufacturer of the lithium foil used in this study (FMC Lithium) lists the concentrations of a number of elements other than lithium. The most abundant element listed, at a concentration of 300 ppm by weight is nitrogen which is probably in the form of Li_3N (refs 29,30). The deposition of lithium on an electrode containing such a contaminant would result in slower deposition in the region near the insulating Li_3N crystallite relative to that in surrounding regions. Figure 4a shows a high-resolution X-ray tomography image of a symmetric lithium–SEO–lithium cell with a crystalline contaminant at the electrode/electrolyte interface. Under low resolution, these crystallites appear as bright specks in the lithium electrode and are clearly visible in Supplementary Video 3. Every dendritic structure that we have observed seems to have a bright speck at the base. Examples of X-ray tomograms emphasizing the bright specks at the base of dendrites are shown in Fig. 4b. Our results suggest that eliminating insulative contaminants from the lithium electrodes is the key to solving the lithium dendrite problem in polymer electrolytes. More work is needed to establish a general framework for understanding the relationship between dendrite formation in lithium electrodes and properties of the electrolyte (for example viscosity, modulus, salt concentration and so on). Previous work[9,11,31,32] provides a starting point for developing such a framework, including the effect of lateral heterogeneity in the electrode on dendrite growth[33].

The growth of dendritic structures from lithium metal anodes is a major problem precluding the widespread use of high-energy-density, rechargeable batteries with lithium metal anodes. Synchrotron hard X-ray microtomography was used to study the morphology of cycled lithium–polymer–lithium cells at 90 °C. The data show conclusively that under these conditions, buried under every dendritic structure emanating from the electrode/electrolyte interface, were subsurface structures located within the lithium electrode. In the early stages of dendrite formation, the volume occupied by the subsurface structure is significantly larger than that occupied by the dendritic structure protruding out from the electrode surface. Present approaches for preventing dendrite growth on lithium metal electrodes are based primarily on suppressing the protrusions. This work indicates the need for a fresh start; preventing the growth of lithium dendrites may involve suppressing the nucleation of subsurface structures in the lithium electrode itself, long before the dendrites extend into the electrolyte.

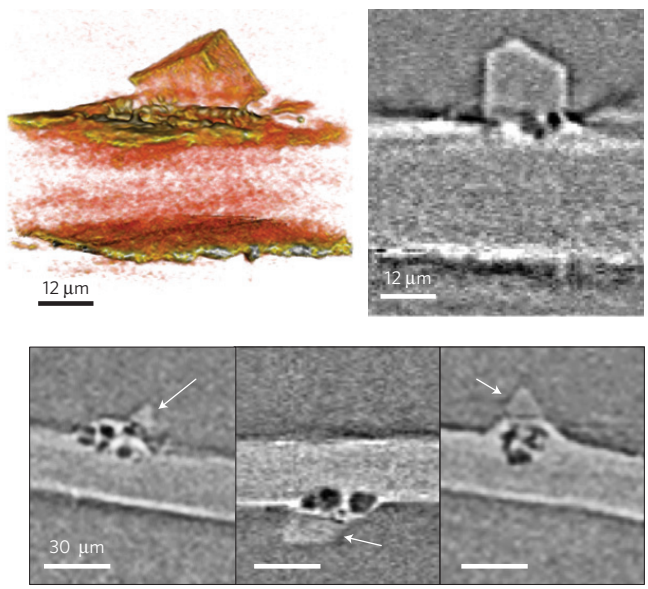

Figure 4 | Crystallites at base of dendrites. a, A high-magnification image (right) and its corresponding 3D reconstruction (left) of a crystallite sitting at the SEO electrolyte/lithium metal electrode interface. This cell was cycled to $C = 18\ C\ cm^{-2}$. **b**, X-ray microtomography images of dendrites with crystallites at their base. The first and last images were taken from different locations within the cell cycled to $C = 84\ C\ cm^{-2}$. The centre image was taken from a cell cycled to $C = 16\ C\ cm^{-2}$. The arrows point to crystallite impurities at the base of the dendritic structure.

Methods

Sample preparation. The samples discussed in this study were prepared using the following technique. A polystyrene-block-poly(ethylene oxide) copolymer electrolyte (SEO) was prepared by anionic polymerization, as described in previous work[34–36]. The molar mass of the polystyrene and PEO blocks were 240,000 and 260,000 Da, respectively, with a PEO volume fraction of 0.50 and an overall polydispersity index of 1.26. The copolymer was dissolved in *N*-methylpyrrolidone (NMP) and mixed with LiTFSI salt such that the molar ratio of lithium ions to ethylene oxide groups was 0.085. This salt concentration was found to maximize conductivity in SEO electrolytes[37]. An electrolyte film was then cast with a nickel-foil-coated solvent caster forming a 30-µm-thick sheet after the NMP evaporated away.

In Supplementary Fig. 1a, we show typical results obtained during the first 30 cycles. In Supplementary Fig. 1b, we show typical data from a cell as it shorted. It is clear that the total amount of charge passed through the cell before shorting, C, is easily detected. For the cell in Supplementary Fig. 1b, $C = 593\ C\ cm^{-2}$.

X-ray microtomography. The cells were imaged using monochromatic hard X-rays with energies chosen in the 22–25 keV range on beamline 8.3.2 at the Advanced Light Source at Lawrence Berkeley National Laboratory. X-rays generated by the synchrotron illuminated the entire sample, and the X-ray shadow cast by the sample was converted into visible light using a scintillator. An optical microscope magnified this image and converted it into a digital image file. The sample was then rotated by a fraction of a degree and repeatedly imaged until 1,025 images were collected from the sample as it was rotated through 180°. After a series of data processing steps, these shadow images were converted to cross-sectional slices that were then stacked together to render a 3D reconstruction of the cell.

Methods for calculating dendrite volume. For the case of the non-electrolyte-spanning dendritic structures (for example, Fig. 1c) we approximate that each structure is composed of two half-ellipsoids. The half-ellipsoid in the lithium electrode has characteristic lengths a, b_l and c. The half-ellipsoid in the polymer electrolyte has characteristic lengths a, b_p and c. We obtained these lengths by examining our images in a Cartesian coordinate system defined in Supplementary Fig. 4. Also shown in Supplementary Fig. 4 is a magnified view of a particular slice through the dendritic structure shown in Fig. 1c. The electrode/electrolyte interface is approximately parallel to the xz plane. We examined xy slices at various z locations and found the slice that contains the largest number of dendritic voxels. We refer to this location as $z = z_D$. We assume that the length of the structure along the

x-direction is $2a$. The half-minor-axes of the two half-ellipsoids are depicted by line segments $\overline{AD}$ and $\overline{DB}$ in Supplementary Fig. 4. The plane of the interface between the electrode and the electrolyte within the dendritic structure is determined by extrapolating the line that defines the interface away from the structure in the $z = z_D$ plane as shown in Supplementary Fig. 4. This plane intersects $\overline{AB}$ at point D.

$$b_p = m(\overline{AD})$$
$$b_l = m(\overline{DB})$$

where subscripts p and l stand for polymer electrolyte and lithium electrode. We then examine xy slices in the $z < z_D$ regime until the structure disappears at $z = z_{Df}$. Similarly, we examine xy slices in the $z > z_D$ regime until the structure disappears at $z = z_{Db}$. We take $2c = |z_{Df} - z_{Db}|$. The volume of the dendritic structure in the phase of interest is given by $V_i = (2/3)\pi ab_i c$, where $i =$ p or l. We define ρ to be the ratio of the volume of the dendritic structure in the electrolyte to the volume in the electrode ($\rho = V_p/V_l$).

PEO cycling. A symmetric lithium–PEO–lithium cell was prepared by pressing homopolymer PEO, molar mass 240,000 Da, into a 3/16-inch-diameter spacer cut from pouch material. Two pieces of lithium foil were placed on either side of the PEO film. The cell was vacuum sealed and then cycled at 90 °C on a Bio-Logic VMP3 at atmospheric pressure. The cycling routine was as follows. The cells were first cycled 15 times at a low current density of 0.06 mA cm^{-2}. This was followed by cycling at a current density of 0.175 mA cm^{-2}. After 23 cycles at 0.175 mA cm^{-2}, the current density was increased to 0.34 mA cm^{-2} for two cycles, at which point the cell shorted. X-ray tomographs of the shorted cell were compared with an uncycled lithium–PEO–lithium cell prepared in the same manner. No structures like those seen in Supplementary Fig. 2 were visible in the uncycled cell.

Received 23 January 2013; accepted 1 October 2013; published online 24 November 2013

References

1. US Department of Energy *Multi-Year Program Plan 2011–2015: Vehicle Technologies Program.* (2010).
2. Tarascon, J. M. & Armand, M. Issues and challenges facing rechargeable lithium batteries. *Nature* **414,** 359–367 (2001).
3. Yaws, C. L. *Yaws' Handbook of Properties of the Chemical Elements* (Knovel, 2011).
4. Aurbach, D., Zinigrad, E., Cohen, Y. & Teller, H. A short review of failure mechanisms of lithium metal and lithiated graphite anodes in liquid electrolyte solutions. *Solid State Ion.* **148,** 405–416 (2002).
5. Eweka, E., Owen, J. R. & Ritchie, A. Electrolytes and additives for high efficiency lithium cycling. *J. Power Sources* **65,** 247–251 (1997).
6. Goodenough, J. B. & Kim, Y. Challenges for rechargeable Li batteries. *Chem. Mater.* **22,** 587–603 (2010).
7. Kalnaus, S., Sabau, A. S., Tenhaeff, W. E., Dudney, N. J. & Daniel, C. Design of composite polymer electrolytes for Li ion batteries based on mechanical stability criteria. *J. Power Sources* **201,** 280–287 (2012).
8. Tatsuma, T., Taguchi, M., Iwaku, M., Sotomura, T. & Oyama, N. Inhibition effects of polyacrylonitrile gel electrolytes on lithium dendrite formation. *J. Electroanal. Chem.* **472,** 142–146 (1999).
9. Monroe, C. & Newman, J. Dendrite growth in lithium/polymer systems—A propagation model for liquid electrolytes under galvanostatic conditions. *J. Electrochem. Soc.* **150,** A1377–A1384 (2003).
10. Mayers, M. Z., Kaminski, J. W. & Miller, T. F. Suppression of dendrite formation via pulse charging in rechargeable lithium metal batteries. *J. Phys. Chem. C* **116,** 26214–26221 (2012).
11. Monroe, C. & Newman, J. The impact of elastic deformation on deposition kinetics at lithium/polymer interfaces. *J. Electrochem. Soc.* **152,** A396–A404 (2005).
12. Gellings, P. J. & Bouwmeester, H. J. M. *The CRC Handbook of Solid State Electrochemistry* (CRC Press, 1997).
13. Bruce, P. G., Freunberger, S. A., Hardwick, L. J. & Tarascon, J. M. Li–O_2 and Li–S batteries with high energy storage. *Nature Mater.* **11,** 19–29 (2012).
14. Dunn, B., Kamath, H. & Tarascon, J. M. Electrical energy storage for the grid: A battery of choices. *Science* **334,** 928–935 (2011).
15. Gireaud, L., Grugeon, S., Laruelle, S., Yrieix, B. & Tarascon, J. M. Lithium metal stripping/plating mechanisms studies: A metallurgical approach. *Electrochem. Commun.* **8,** 1639–1649 (2006).
16. Brissot, C., Rosso, M., Chazalviel, J. N. & Lascaud, S. *In situ* concentration cartography in the neighborhood of dendrites growing in lithium/polymer-electrolyte/lithium cells. *J. Electrochem. Soc.* **146,** 4393–4400 (1999).
17. Rosso, M. *et al.* Dendrite short-circuit and fuse effect on Li/polymer/Li cells. *Electrochim. Acta* **51,** 5334–5340 (2006).
18. Stone, G. M. *et al.* Resolution of the modulus versus adhesion dilemma in solid polymer electrolytes for rechargeable lithium metal batteries. *J. Electrochem. Soc.* **159,** A222–A227 (2012).
19. Liu, S. *et al.* Lithium dendrite formation in Li/poly(ethylene oxide)-lithium bis(trifluoromethanesulfonyl)imide and *N*-methyl-*N*-propylpiperidinium bis(trifluoromethanesulfonyl)imide/Li cells. *J. Electrochem. Soc.* **157,** A1092–A1098 (2010).
20. Dolle, M., Sannier, L., Beaudoin, B., Trentin, M. & Tarascon, J. M. Live scanning electron microscope observations of dendritic growth in lithium/polymer cells. *Electrochem. Solid State* **5,** A286–A289 (2002).
21. Bhattacharyya, R. *et al. In situ* NMR observation of the formation of metallic lithium microstructures in lithium batteries. *Nature Mater.* **9,** 504–510 (2010).
22. Chandrashekar, S. *et al.* Li-7 MRI of Li batteries reveals location of microstructural lithium. *Nature Mater.* **11,** 311–315 (2012).
23. Tatsuma, T., Taguchi, M. & Oyama, N. Inhibition effect of covalently cross-linked gel electrolytes on lithium dendrite formation. *Electrochim. Acta* **46,** 1201–1205 (2001).
24. Lopez, C. M., Vaughey, J. T. & Dees, D. W. Morphological transitions on lithium metal anodes. *J. Electrochem. Soc.* **156,** A726–A729 (2009).
25. Yoshimatsu, I., Hirai, T. & Yamaki, J. Lithium electrode morphology during cycling in lithium cells. *J. Electrochem. Soc.* **135,** 2422–2427 (1988).
26. MacDowell, A. A. *et al.* X-ray micro-tomography at the Advanced Light Source. *Proc. SPIE* **8506,** 850618 (2012).
27. Groso, A. *et al.* Phase contrast tomography: An alternative approach. *Appl. Phys. Lett.* **88,** 214104 (2006).
28. Maia, F. R. N. C. *et al.* Compressive phase contrast tomography. *Proc. SPIE* **7800,** 78000F (2010).
29. Lectro Max 100 Product Data Sheet; http://www.fmclithium.com/
30. Frianeza-Kullberg, T. C. & Salmon, D. J. Removal of lithium nitride from lithium metal. US patent 4,781,756 (1988).
31. Brissot, C., Rosso, M., Chazalviel, J. N. & Lascaud, S. in *Studies in Surface Science and Catalysis* Vol. 132 (eds Oyama, N., Iwasawa, Y. & Hironobu, K.) 947–952 (Elsevier, 2001).
32. Rosso, M., Chassaing, E., Chazalviel, J. N. & Gobron, T. Onset of current-driven concentration instabilities in thin cell electrodeposition with small inter-electrode distance. *Electrochim. Acta* **47,** 1267–1273 (2002).
33. Rosso, M., Gobron, T., Brissot, C., Chazalviel, J. N. & Lascaud, S. Onset of dendritic growth in lithium/polymer cells. *J. Power Sources* **97–98,** 804–806 (2001).
34. Mullin, S. A., Stone, G. M., Panday, A. & Balsara, N. P. Salt diffusion coefficients in block copolymer electrolytes. *J. Electrochem. Soc.* **158,** A619–A627 (2011).
35. Singh, M. *et al.* Effect of molecular weight on the mechanical and electrical properties of block copolymer electrolytes. *Macromolecules* **40,** 4578–4585 (2007).
36. Bruce, P. G. & Vincent, C. A. Polymer electrolytes. *J. Chem. Soc. Faraday Trans.* **89,** 3187–3203 (1993).
37. Panday, A. *et al.* Effect of molecular weight and salt concentration on conductivity of block copolymer electrolytes. *Macromolecules* **42,** 4632–4637 (2009).

Acknowledgements

Primary financial support for the work was provided by the Electron Microscopy of Soft Matter Program from the Office of Science, Office of Basic Energy Sciences, Materials Sciences and Engineering Division of the US Department of Energy under Contract No. DE-AC02-05CH11231 and the BATT programme from the Vehicle Technologies programme, through the Office of Energy Efficiency and Renewable Energy under US DOE Contract DE-AC02-05CH11231. Hard X-ray microtomography experiments were performed at the Advanced Light Source, which is supported by the Director, Office of Science, Office of Basic Energy Sciences, of the US Department of Energy under Contract No. DE-AC02-05CH11231. K.J.H. was supported by a National Science Foundation Graduate Research Fellowship.

Author contributions

K.J.H. and D.T.H. prepped samples and performed the experiments. D.Y.P. and A.A.M. aided in synchrotron experimental set-up and discussion of results. K.J.H. and N.P.B. prepared figures and composed the manuscript. N.P.B. directed the work.

Additional information

Supplementary information is available in the online version of the paper. Reprints and permissions information is available online at www.nature.com/reprints. Correspondence and requests for materials should be addressed to N.P.B.

Competing financial interests

The authors declare no competing financial interests.